Environmental scanning electron microscopy (ESEM) and nanoindentation investigation of the crack tip process zone in marble

Environmental Scanning Electron Microscopy (ESEM) and Nanoindentation Investigation of the Crack Tip Process Zone in Marble

Z. Brooks · **F.-J. Ulm** · **H.H. Einstein**

Abstract This study explores the interaction between crack initiation and nanomechanical properties in the crack tip fracture process zone of Carrara marble. Specimens with pre-existing cracks were loaded in a uniaxial testing machine until the process zone appeared at the tips of the pre-existing cracks. ESEM analysis reveals an increase in microcrack density in the process zone with increased loading of the specimen. Nanoindentation testing comprised of lines and grids of single nanoindentations located both near and far from the process zone show a decrease of both indentation modulus and indentation hardness near grain boundaries in intact material, and with closeness to the process zone. Ultimately, the study confirms that the crack tip process zone manifests itself as an area of reduced indentation hardness and indentation modulus in marble.

Keywords Nanoindentation · Environmental Scanning Electron Microscopy (ESEM) · fracture process zone · Carrara Marble

1 Introduction

The determination of the mechanisms at play during crack propagation is one of the key challenges in the field of fracture mechanics of rocks. The principles of Linear Elastic Fracture Mechanics (LEFM) dictate that fracture propagation critera (such as either local stress-intensity criteria, or global energy release criteria) should be used to consider the otherwise infinite stresses at the tip of an ideal crack [16, 19, 20]. Another way to reflect these conditions is through the fracture process zone (FPZ) as suggested by Irwin, Barenblatt and Dugdale [7, 14, 20, 21]. The FPZ develops in the near-crack-tip region when the stress reaches the value of the material strength. At this point, the material yields to form a damage zone termed the FPZ [18]. *(Addresses comments (1) and (3).)* Researchers have found significant interest in the detailed experimental investigation of the FPZ in order to determine its precise effect on the material behavior. In metals, the FPZ is often known as the "plastic zone". Strain-hardening metals produce an increase in hardness within the plastic zone, and strain-softening metals produce a decrease [32]. The development of strength and deformability in the FPZ is not clearly established for brittle and quasi-brittle materials and is the subject of this investigation. By specifically studying microstructure, such a finding might allow one to relate material property changes to the FPZ in such material.

Microscale experimental investigation of the FPZ in brittle and quasi-brittle materials chiefly uses four techniques: microscopy [3, 19, 29], interferometry [10–12, 14, 28], acoustic emission [6, 18, 21, 25, 27, 40], and ultrasonic pulses [20, 30, 38]. Although these techniques provide important information on the microstructure of the FPZ – in particular, the exponential increase of microcrack density within the FPZ with closeness to the main crack or fault – they fail to directly measure material properties within the FPZ. Additionally, the studies typically focus on heterogenous materials such as granite, concrete, and natural faults in a variety of rock materials. Although such materials are important from an engineering perspective, a study in a geomaterial with minimal variety of constituents will remove the effect of material heterogeneity on FPZ development. Study of a mono-mineral geomaterial can isolate ~~and illuminate~~ the ~~true~~ effects of the FPZ on material properties. *(Addresses Comment (4).)* Thus, a need exists for an experimental technique that will directly yield properties in the FPZ of a quasi-brittle, mineralogically homogeneous material. This investigation pursues material properties and microstructure change in the FPZ of Carrara marble. Marble physically brightens, or displays "white patching" at the tips of existing cracks prior to the growth of new cracks (Figure 1).

Z. Brooks
77 Massachusetts Ave, Rm 1-331
Tel.: 617.253.7101
Fax: 617.258.6775
E-mail: zbrooks@mit.edu

F.-J. Ulm
77 Massachusetts Ave, Rm 1-263
Tel.: 617.253.3544
Fax: 617.258.6775
E-mail: ulm@mit.edu

H.H. Einstein
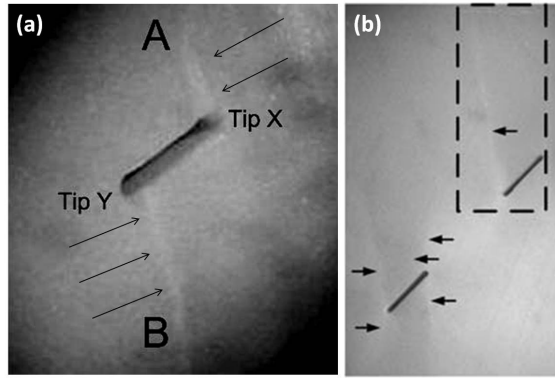77 Massachusetts Ave, Rm 1-342
Tel.: 617.253.3598

Fig. 1: Loading of a marble specimen with one (a) or two (b) pre-existing cracks generates white patching, indicated by black arrows in the figure. (a) From [35]. (b) (With kind permission from Springer Science+Business Media: [37], Figure 1(a).)
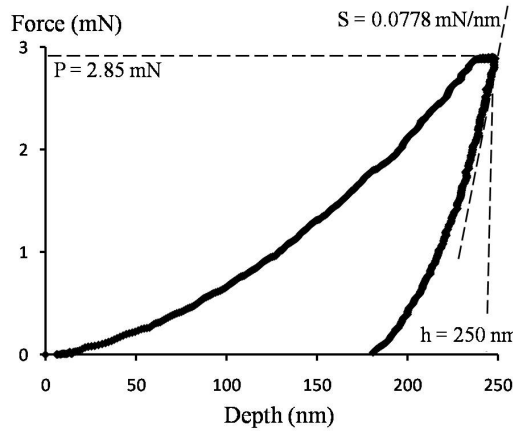

Fig. 2: Force-indentation depth curve of an indentation test into marble. The important physical quantities which determine indentation modulus and hardness are obtained from this curve.

Wong [35–37] was able to qualitatively relate this white patching to the development of microcracks. The current study aims at investigating in detail the micro- and nanomechanical properties of this type of near-crack-tip FPZ.

The nanoindentation test is a small scale indentation test which yields nanomechanical properties of the test material [7, 8]. A diamond-tipped indenter pushes onto a specimen surface at a specified loading rate and peak load. A force-depth curve (P-h) is recorded (Figure 2). The application of continuum-scale contact models to the indentation test condenses the P-h curve into two quantities; the indentation modulus M:

$$M = \frac{1}{2} S \sqrt{\frac{\pi}{A_c}}, \tag{1}$$

and the indentation hardness H:

$$H = \frac{P_{\max}}{A_c}, \tag{2}$$

where S is the initial slope of the unloading curve; P_{max} is the peak load, and A_c is the (projected) contact area at peak load, which can also be determined from the maximum indentation depth upon unloading [26]. These nanomechanical properties – modulus and hardness – represent material stress-strain and strength behavior. In fact, the indentation modulus is an indicator of elasticity, and coincides, in the isotropic case, with the plane-stress modulus of elasticity,

$$M = \frac{E}{1 - \nu^2}. \tag{3}$$

In turn, the indentation hardness is related to the maximum stress sustained by the material before undergoing plastic deformation [13], and is thus an indicator of the material's strength.

This investigation explores the nanomechanical properties of the FPZ in marble. It is the first study doing this specifically in natural geomaterials. This investigation makes three major comparisons of nanomechanical properties:

1. at different orientations in the marble block,
2. between grain center and grain boundary (in both "intact" and FPZ marble), and
3. between "intact" and FPZ marble.

Fax: 617.258.6775
E-mail: einstein@mit.edu

across four marble specimens. Due to the natural variability in properties between marble specimens, "intact" nanomechanical values are interpreted from nanoindentations at a distance from the FPZ. These comparisons are supplemented with a microstructure study via Environmental Scanning Electron Microscopy (ESEM). The third comparison is the most encompassing and important of the four; this comparison provides a basis for determining not only the difference between intact and FPZ marble, but also what underlying FPZ mechanisms are responsible for this difference.

2 Materials and Experiments

2.1 Materials

The experimental material for this study is marble from quarries near the town of Carrara, in the northwestern part of the Alpi Apuane metamorphic complex in Italy (See the box indicated in Figure 3). The precise location is displayed in Figure 4. Typical material properties are listed in Table 1.

Previous work on Carrara marble presented both macroscale and microscale information of the FPZ in marble [35–37], and linked macroscale crack propagation and crack coalescence in gypsum and marble specimens with various pre-existing crack ("flaw") geometries by means of digital photography. As briefly mentioned before, those studies noted that marble physically brightens, or displays "white patching" at the tips of flaws prior to crack propagation (Figure 1). White patching was then investigated at the microscale with scanning electron microscopy; the study found that white patches result from the growth and extension of networks of inter- and intragranular microcracks (Figure 5), which were described with four qualitative densities: Background (natural density of microcracks in the intact rock), Low, Medium, and High Crack Density. For our study we consider this white patching region as an FPZ in marble because it contains microstructural FPZ features (i.e., microcracks) and, very importantly, precedes the development of a macroscale crack.

The size of the FPZ regions investigated in this study fell within the bounds of the process zone size – the radial distance from the pre-existing crack tip within which material has yielded, r_p. This expression for r_p is developed from crack-tip stress field solutions developed by Irwin [16] for "somewhat brittle" materials (i.e., materials where the region of plastic deformations is small relative to crack length):
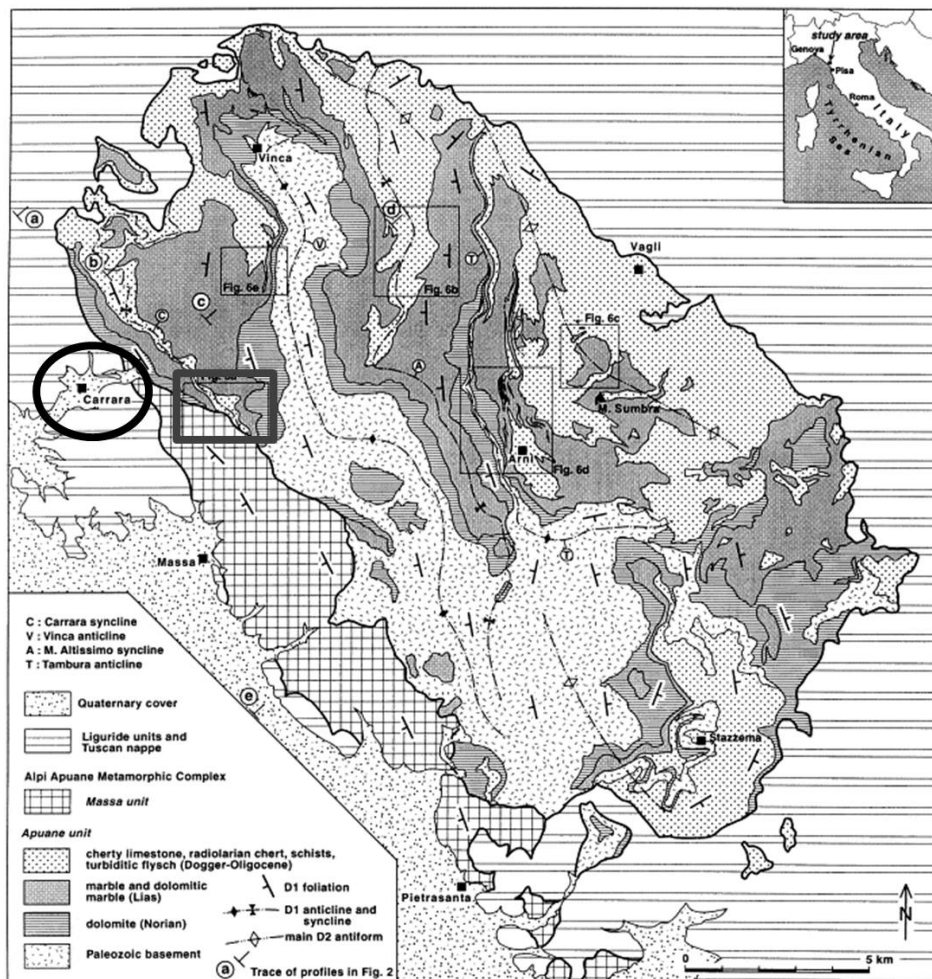

Fig. 3: The Alpi Apuane marble complex in northern Italy. The town of Carrara is circled on the left. Details of the boxed inset are shown in Figure 4. (Reprinted from [24], with permission from Elsevier.)
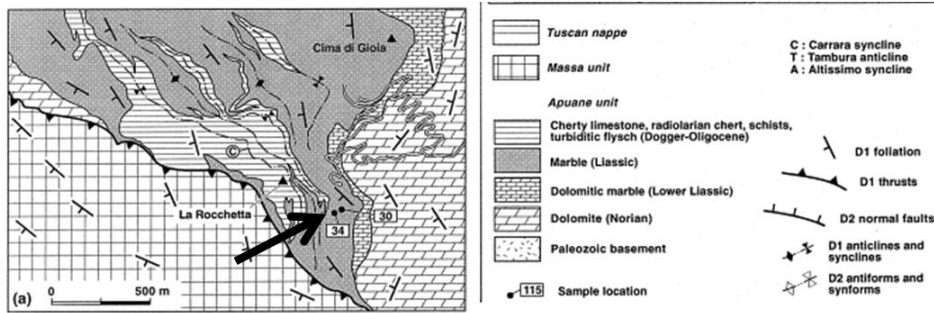
3

Fig. 4: Close-up of the boxed region in Figure 3. The arrow indicates the precise origin of the marble used in the study, the normal limb of a northest- facing isoclinal fold. (Reprinted from [24], with permission from Elsevier.)

Table 1: Typical properties of Carrara marble.

| Property	Value	Source
Chief Constituents	Calcium Carbonate (CaCO$_3$)	
Other Constituents	Organic Foliation, Quartz, Albite, White Mica, Opaque Minerals	
Fabric	Homogenous; no preferred grain shape or crystallographic orientation	
Grain Size	40-200 μm	[24]
Young's Modulus, E	49 GPa	[35]
Poisson's ratio, ν	0.19	[35]
Porosity	0.33 - 0.48	[2]
Uniaxial Compressive Strength, σ_c	33.85 MPa	[35]
Flexural Strength	13 MPa	[22]
Tensile Strength, σ_{yt}	3.32 to 5.86 MPa	[9, 39]
Fracture Toughness, K_{Ic}	0.65 to 1.25MPa$\sqrt{m}$	[1, 4]
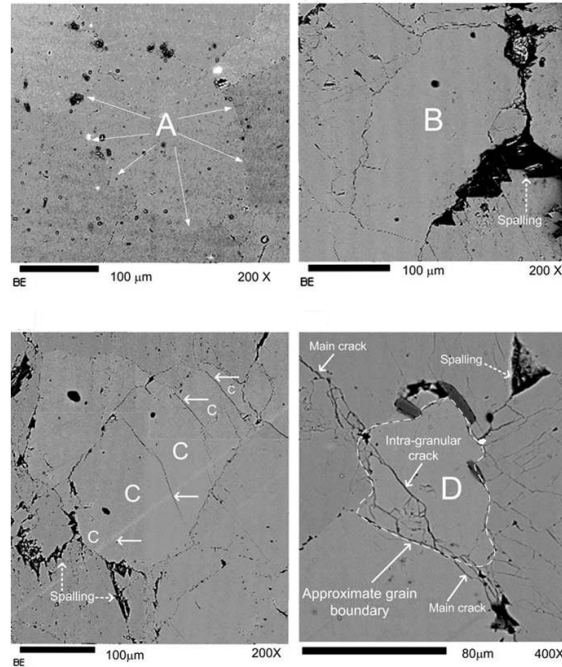
Fig. 5: Established microstructural features of the FPZ viewed with standard Scanning Electron Microscopy. a) Intact marble grain b) Intergranular cracking c) Spalling d) Intergranular and intragranular cracking. (With kind permission from Springer Science+Business Media: [37], Figure 7.)

$$r_p = \frac{1}{2\pi}\left(\frac{K_{Ic}}{\sigma_0}\right)^2, \tag{4}$$

where K_{Ic} is the material fracture toughness, and σ_0 is the material yield strength [15]. Carrara marble exhibits a typical fracture toughness of $K_{Ic} = 0.65$ to 1.25 MPa$\sqrt{m}$ [1, 4] and a tensile strength of $\sigma_0 = 3.32$ to 5.86 MPa[9, 39]; these material properties yield an estimated LEFM process zone size of $r_p = 0.19$ to 2.3 cm for a Mode I crack in Carrara marble [2, 17]. Note that this expression is typically applied to metallic materials [37], but is applied to quasi-brittle materials in this investigation as a rough approximation of process zone size (which guides nanoindentation testing locations.)

For this investigation, white patching indicated the FPZ. Linear white patches extended from pre-existing cracks to near the specimen boundary. Nanoindentations and ESEM observation were conducted in parallel on observed white patching, within regions at a distance of less than 1 mm to no more than 7 mm from the observed white patching. Thus, investigations discussed in Section 2.2 occurred well within the theoretically defined range.

2.2 Experiments

Specimen Preparation

Table 2: Specimens, the comparisons made on each specimen, and the regions extracted from each specimen. Specimens and regions are illustrated in Figure 6.

Specimen	Comparisons Made on Specimen	Regions Extracted from Specimen
c0	1. at different orientations	c0-x c0-y c0-z
c1	2. between grain boundary and grain center 3. between "intact" and process zone	c1-z1 c1-z2 c1-z3 c1-x c1-y
c2	3. between "intact" and process zone	c2-z
c3	*ESEM only*	c3-y

The specimens studied in this investigation are shown in Figure 6 and listed in Table 2. These specimens were prepared in the following manner. Slices of marble were cut from a Carrara marble slab with a Covington Engineering Heavy Duty Slab Saw (Figure 7a). The slices of marble were then trimmed into 6" x 3" x 1.5" (15.2 cm x 7.6 cm x 3.8 cm) block specimens with an OMAX© Water Jet (Figure 7b, 7c). To have a basis for comparison, the dimensions were equal to those of a previous study [36, 37]. In order to generate different types of loading, four specimens were prepared: Specimen c0, Specimen c1, Specimen c2, and Specimen c3 (Figure 6). No flaw was cut into Specimen c0. An initial crack, or "flaw", oriented at $30°$ from the horizontal axis was cut into Specimens c1, c2, and c3 with the OMAX© Water Jet (Figure 8b.) The flaw measures 0.5" (1.27 cm) in length, approximately 1 mm in width, and extends through the depth of the specimen (1.5", or 3.81 cm). White patching was generated in Specimens c1, c2, and c3 by loading them in a uniaxial testing machine (Figures 8 and 9). Steel brush-platens at the top and bottom of the specimen ensured that far-field stresses were homogeneously applied. Each specimen was loaded at a slow initial rate to eliminate seating effects (0.0017 in/sec to 1000 lb, then 0.003 in/sec to 2500 lb), after which loading continued at a constant rate (38.34 lb/sec, or 170.5 N/sec) until failure or the manual stopping of the test. The flaw tip was continuously monitored with a high-resolution Phantom© High-Speed Camera, and high-resolution still pictures were taken as features of interest developed in the specimen, such as the onset of white patching. Note that the observation of the FPZ with the high speed camera is a very unique feature of this investigation and has been discussed in detail by [34, 36, 37]. Specimens c1 and c2 were unloaded once a significant amount of white patching had developed at the flaw tip. Specimen c3 was loaded all the way to failure [35].

Smaller regions for ESEM and nanoindentation testing were extracted from the specimens with the OMAX© Water Jet and diamond drop-saw. Regions and their corresponding specimens are shown in Figure 6 and listed in Table 2 (during extraction with the Water Jet, Regions c1-z1 and c1-z2 (Figure 6) separated along the white patching; these specimens were investigated separately.) The size of the specimens corresponds to the scale of both the observed white patching and the theoretical process zone size predicted by LEFM ($r_p = 0.19$ to 2.3 cm).
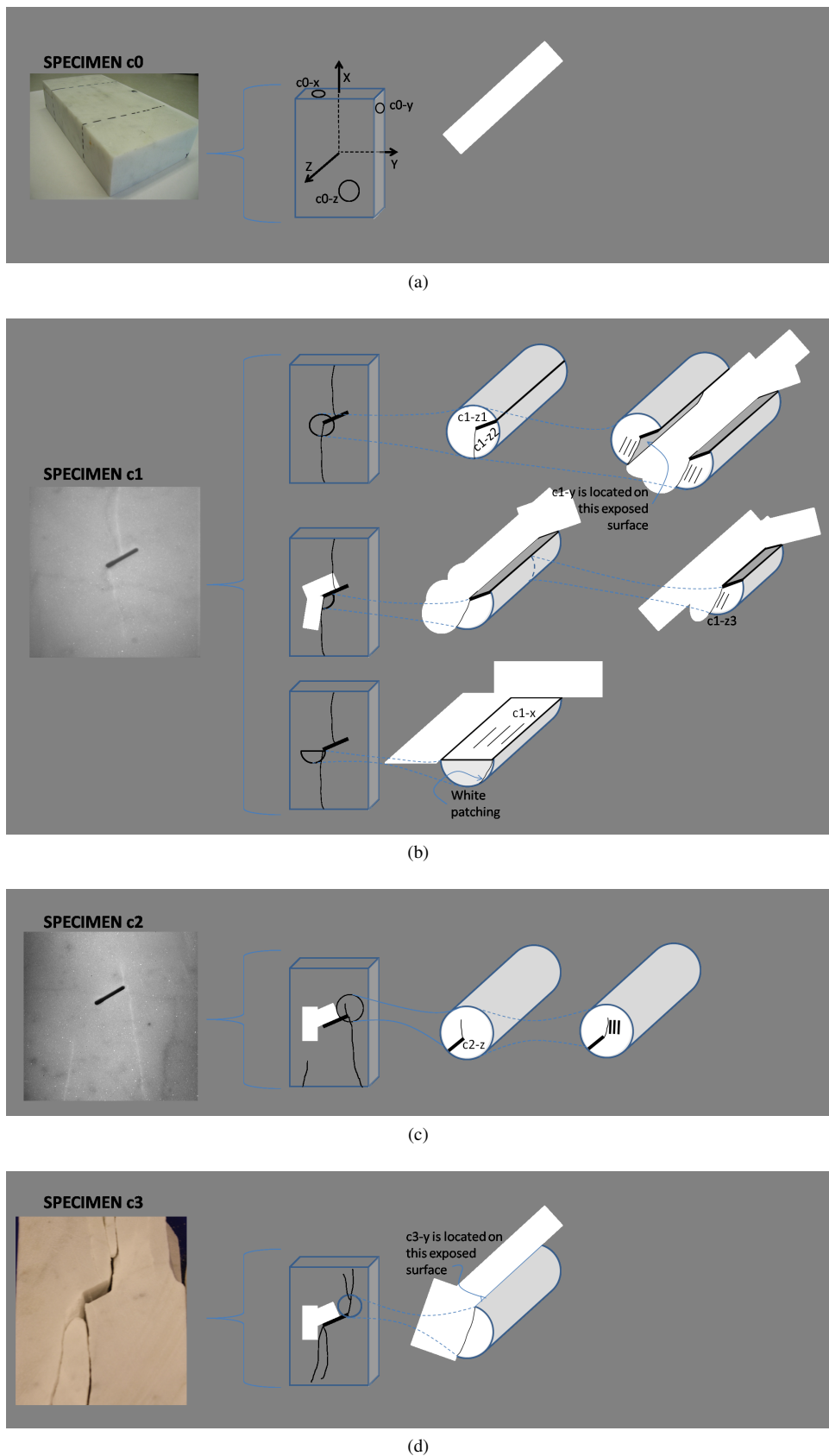
(a)

(b)

(c)

(d)

Fig. 6: Specimens and corresponding regions. The techniques employed on each region are listed in Table 2.
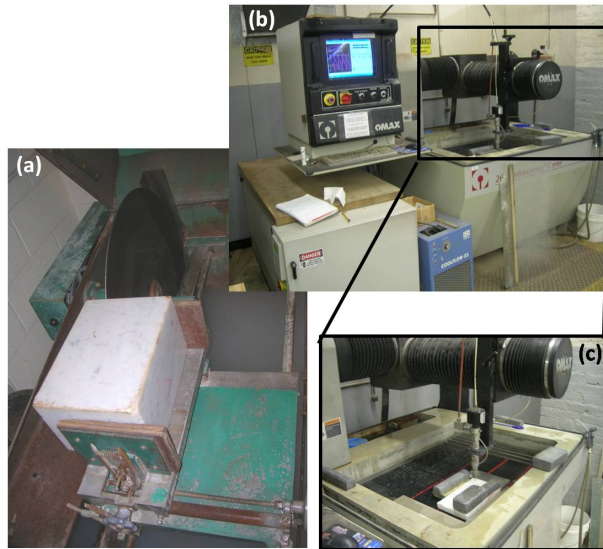
6

Fig. 7: Tools used to cut the specimens: (a) Covington Engineering Heavy Duty Slab Saw, (b) OMAX Water Jet, and (c) close-up of sample prior to cutting in Water Jet.
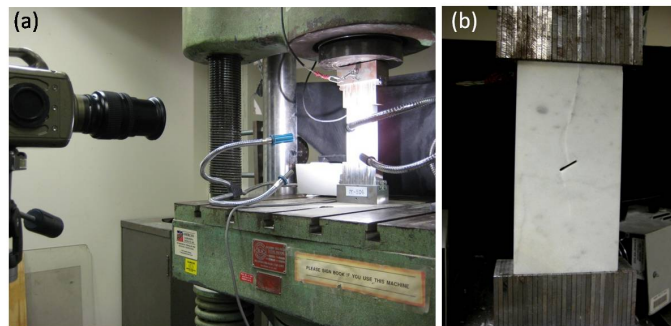

Fig. 8: (a) Typical test setup including Phantom© High-Speed Camera on left, and specimen in uniaxial testing machine on right. (b) Close-up of Process Zone Specimen with steel brush-platens in uniaxial testing machine, post-loading.
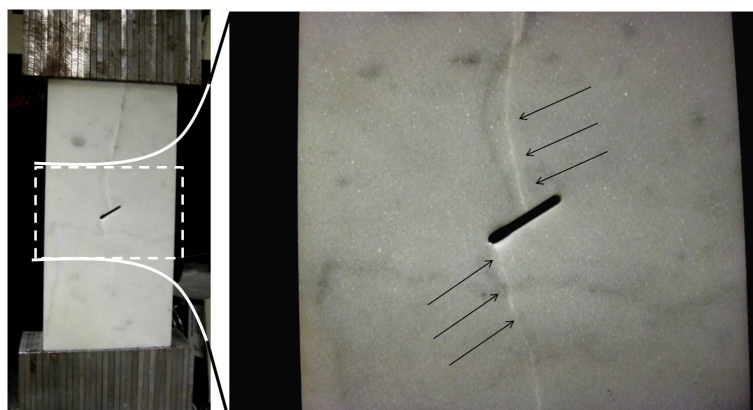

Fig. 9: "White Patching" is visible at and near the tips of the flaw in the Process Zone Specimen. The arrows indicate the white patching.

The testing regions were then mounted on stainless steel Atomic Force Microscopy (AFM) plates with cyanoacrylate, and either observed with ESEM or prepared for nanoindentation (surface preparation is described in Appendix A: Surface Preparation for Nanoindentation). The white patching surface of Regions c1-y and c3-y was visually assessed with an FEI/Philips©XL30 FEG ESEM. Due to the particular imaging technique utilized for imaging of the white patching – ESEM – no surface preparation was necessary before imaging. (For standard SEM, samples must be coated with gold or carbon to assist the electron beam; the use of ESEM eliminates this step and preserves the natural FPZ microstructure.)
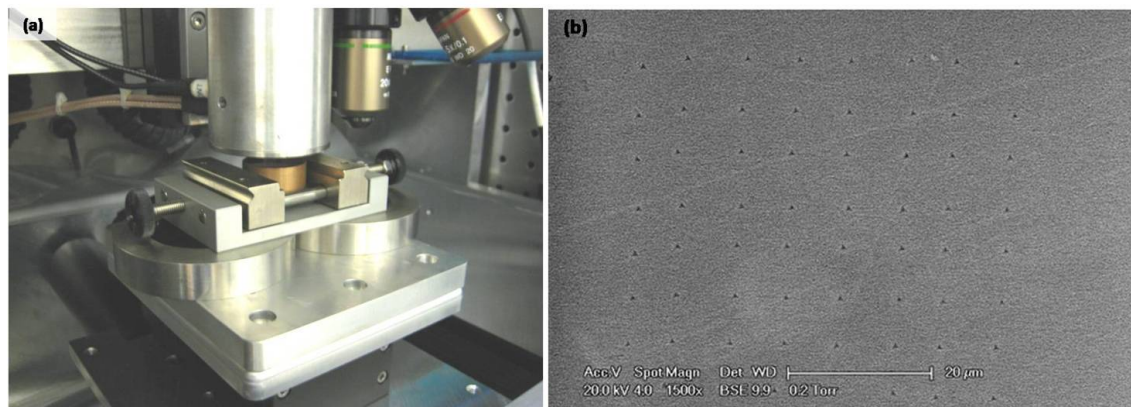
Nanoindentation

Fig. 10: (a) The CSM Instruments Nano-Hardness Tester. (b) An ESEM image of a grid indentation test. Line indentation tests correspond to a single row from a grid indentation test.

Nanoindentations were conducted in a CSM Instruments Nano-Hardness Tester to a maximum load of 2.85 mN, which resulted in a typical indentation depth of 250 nm, and a typical contact area (A in Equation 2) of 0.9 μm^2. For more details on nanoindentation test parameters, see Appendix B. For this investigation, nanoindentations whose load-depth relationship deviated from an approximately second-order shape of the force-displacement curve (as predicted by the classic load-depth relationship derived by Sneddon for conical indentation; see [26] and displayed in Figure 2) were removed, and not included in the analysis unless noted otherwise.

3 Results

3.1 Microstructure

Process Zone Microstructure

Region c1-y (Figure 6b) was imaged with the ESEM (Figure 11). Observation of this exposed surface of the FPZ yielded an abundance of FPZ microscale features. Specific regions of microcracking (Crack 2, Crack 6, and Crack 7) and debris (Debris 1 and Debris 2) are marked in Figure 11 and displayed at high magnification in Figures 12, 13, and 14. Arrows in these figures indicate microcracks, which are associated with widened grain boundaries.

Spalling is visible in Figure 12a, and, in Figure 12b, other particular features are parallel lines near Crack 6 within the marble grain that indicate the regular crystalline structure of the material. By not polishing the specimen or otherwise preparing the surface for microscopy, which is possible with ESEM, the original crack pattern and surface texture is preserved.
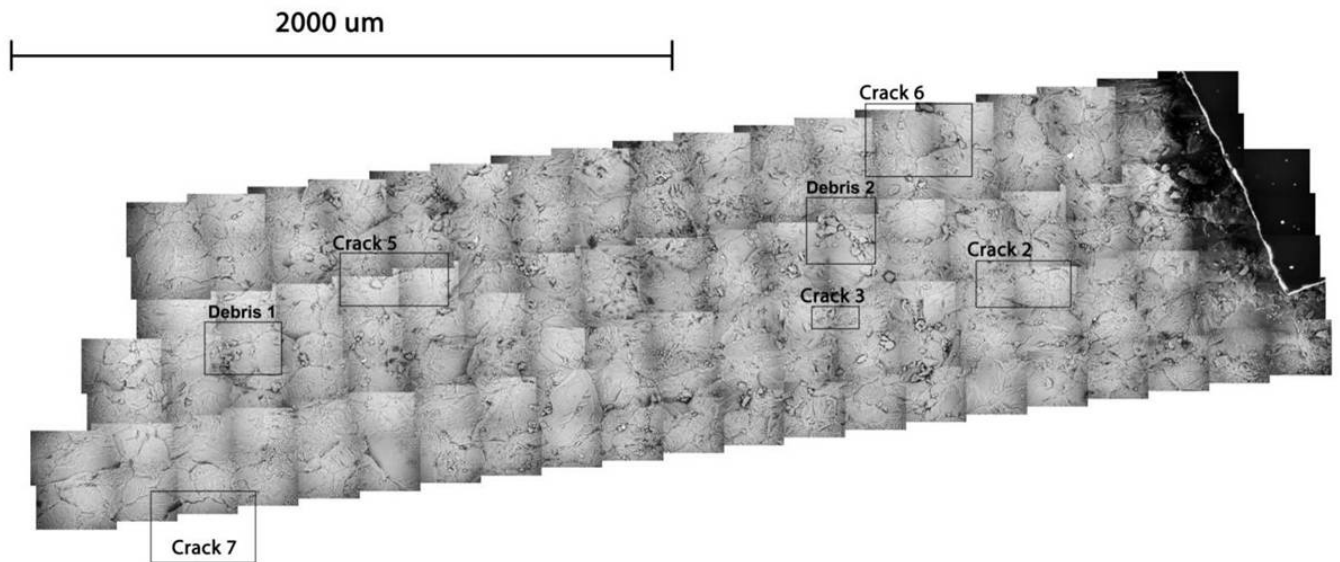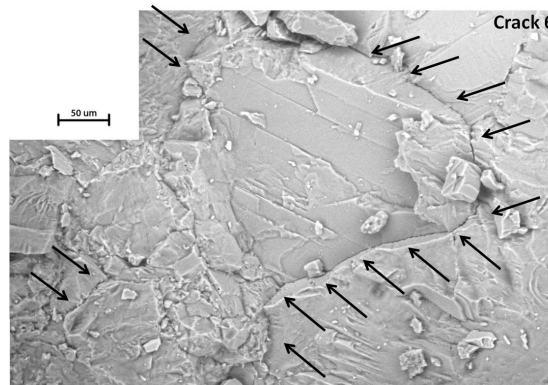
Fig. 11: Region c1-y, from Specimen c1 (Figure 6b). Both microcracks and debris are visible. Detail of boxed areas is presented in the next figures.

(a) Crack 2 from Figure 11.

(b) Crack 6 from Figure 11.

Fig. 12: Microcracks as interpreted from ESEM images; they are usually associated with widened grain boundaries.
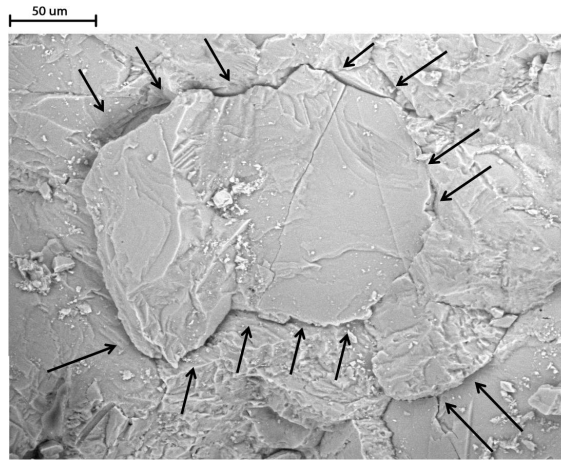
Fig. 13: Crack 7. Particularly on the left edge, the microcrack appears to have dislodged the central marble grain from surrounding marble grains.
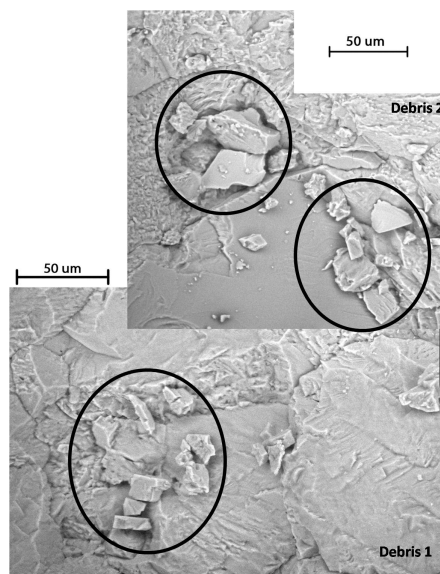

Fig. 14: ESEM does not require surface preparation and thereby can show abraded material on the specimen surface.

As they propagate along grain boundaries, microcracks interact with marble grains, and in some cases may dislodge them from surrounding material and move them upward (Figure 13). The shadow cast on the upper left corner of the marble grain suggests a region of spall. A final feature of interest of many images is the presence of debris, most notable in Figure 14; this debris may also contribute to the white appearance of the FPZ in marble.

Crack Density Analysis

The microcrack density of Region c1-y (Figures 6b and 11) was assessed in order to understand the microstructure of this FPZ region. First, existing qualitative crack density levels were converted to quantitative crack density levels. Wong [35] described four typical crack densities. These densities are shown in the boxes in the upper right corner of Figure 15. For the current study, the actual crack density of each region, total crack per area, was calculated. This calculated density established an upper bound for four quantitative crack density levels. The levels, which are listed in Table 3, were used to evaluate crack density in the current study.
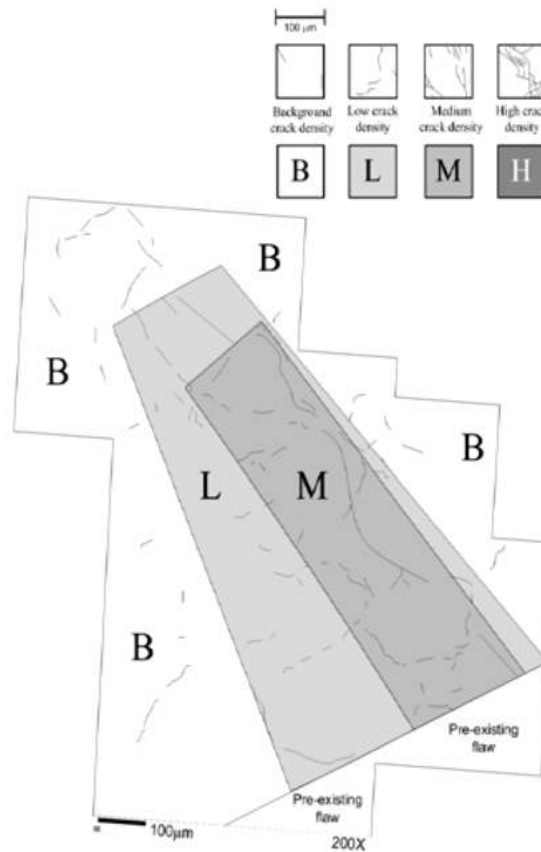

Fig. 15: Four qualitative crack densities. (With kind permission from Springer Science+Business Media: [37], Figure 12(a).)

Table 3: Four quantitative crack densities.

Qualitative Crack Density Level (CDL)	Quantitative CDL (Crack Length in μm per 100^2 μm^2 of Marble)
Background (B)	62.3
Low (L)	169
Medium (M)	391
High (H)	630

Previous work [42] used a 100 μm square to illustrate the different qualitative crack densities (see the scale bar above the crack density boxes, in the upper right corner of Figure 15, from [42].) It was found that a typical Carrara marble grain fit in a square of this size, and that microcracking around the grain was also apparent and traceable in a square of this size. Thus, Region c1-y (Figure 11) was divided into 100 μm x 100 μm square regions and the crack density for each region (total length of microcracking in a single square region) was determined (Figures 16a and 16b). This assessment revealed that only three of the microcrack density levels exist in the imaged area (Figure 16b).
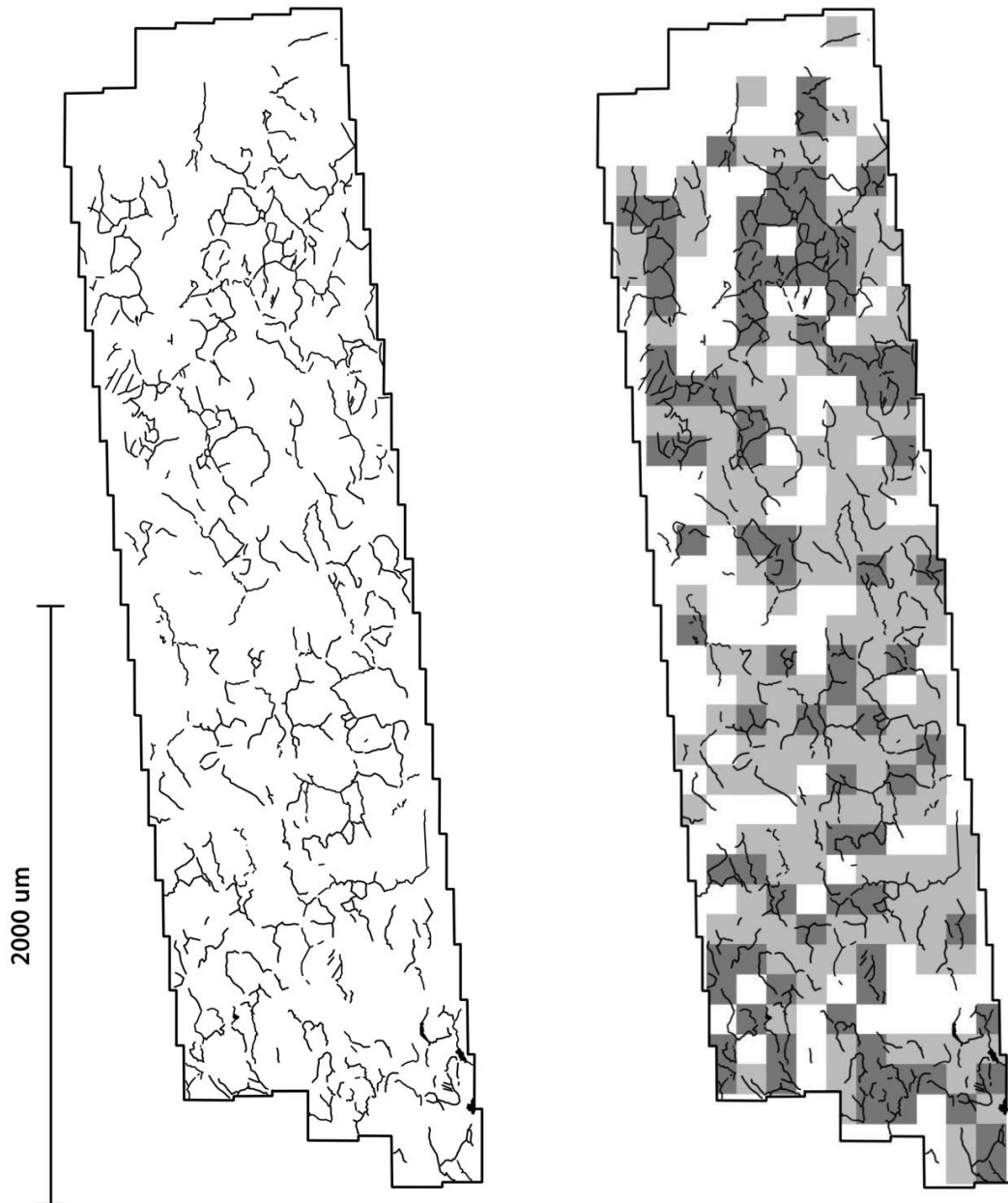
(a) Region c1-y, originally shown in Figure 11, with traced microcracks.

(b) Three of Wong's microcracking densities are found on Region c1-y: Background (no color), Low (light gray), and Medium (dark gray).

Fig. 16: Crack density analysis of Region c1-y.

It was hypothesized that further loading of Specimen c1 would have affected the FPZ, and that assessment of such an FPZ would reveal regions of high crack density. This hypothesis was tested by observing the microstructure of another specimen from a previous study [35] loaded to failure (Figure 17).

Averaged over the entire image, there is an average of 134 μm of crack length per 100^2 μm^2 of material, which also corresponds to Low CDL. Whereas analysis of the FPZ region in Figure 16b yielded three different crack densities (Background, Low, and Medium), analysis of the FPZ region of a higher-loaded specimen yielded all four different crack densities (Background, Low, Medium, and High).

It should be noted that crack density analyses of Figure 17a, shown in Figure 17b, and of Figure 11, shown in Figure 16, account for the length of cracks, but not the width of the crack openings. Thus, cracks that have opened very wide will not be represented by an increased CDL with respect to thinner cracks of the same length. A more comprehensive analysis would account for both length and width of cracks. Thus, the microstructure analyses performed on the specimens in this study represent a first-order approach to crack density analysis, and ultimately reveals trends in crack length density but not total crack width.

With this caveat in mind, the analysis shown in Figure 17 suggests that high loading produces more and longer cracks. *(Addresses Comment (5).)*
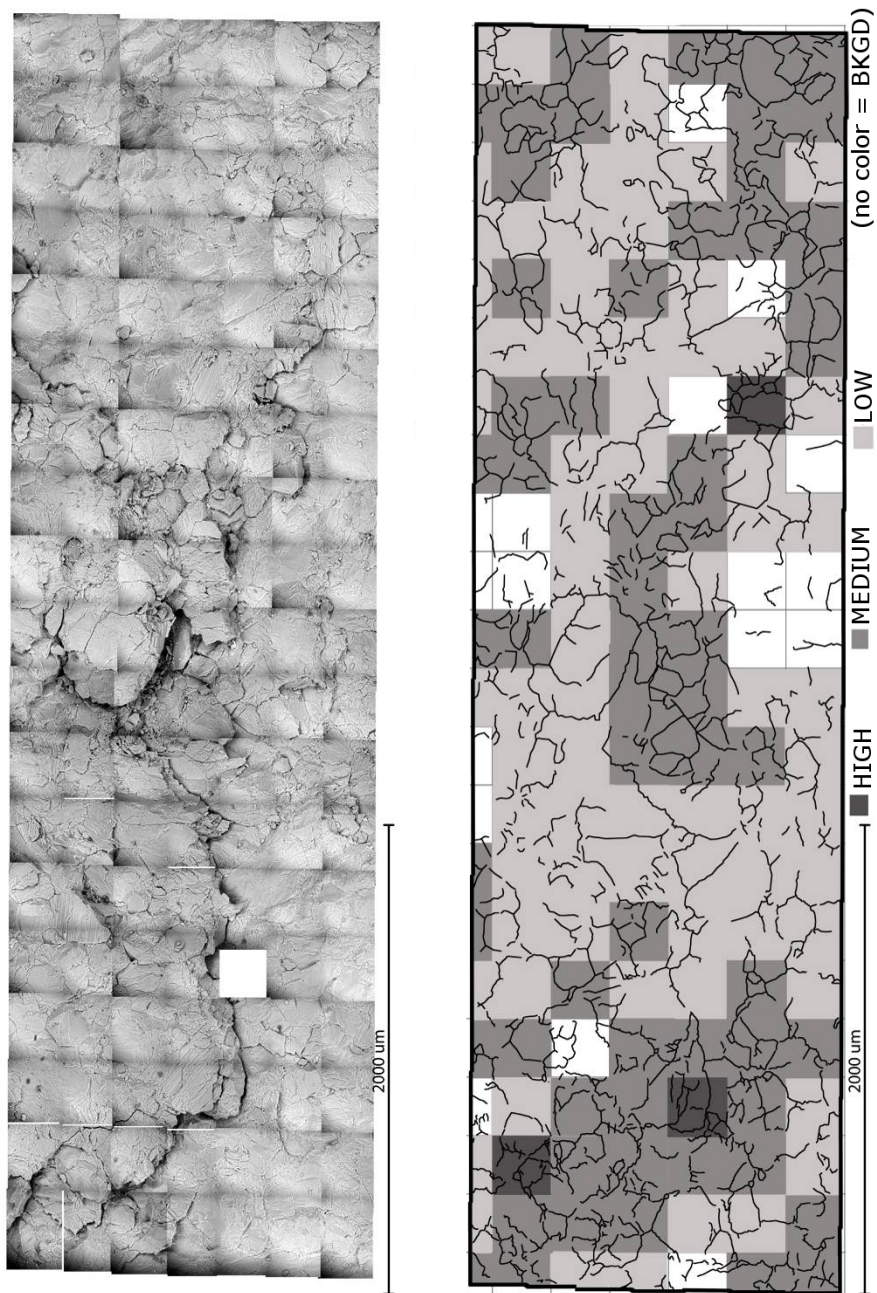
(a) Both microcracks and naturally abraded debris are visible in the exposed white patching surface of the specimen loaded to failure. The density of microcracks is presented in Figure 17b.

(b) The variation in microcrack densities from Figure 17a.

Fig. 17: Crack density analysis of Region c3-y.

3.2 Nanoindentation

Weak Anisotropy of Intact Marble

In order to check for possible anisotropy of intact marble, 478 nanoindentations in grid formation were conducted on three orthogonal faces of Specimen c0 (Figure 6a). Inspection of the nanoindentation results (Figure 18; see Appendix C for an explanation of boxplots as presented in this investigation) reveals a higher indentation modulus and indentation hardness (73.52 GPa indentation modulus, and 2.98 GPa indentation hardness) on the Z-face (i.e., the face to which the Z-axis is normal) compared
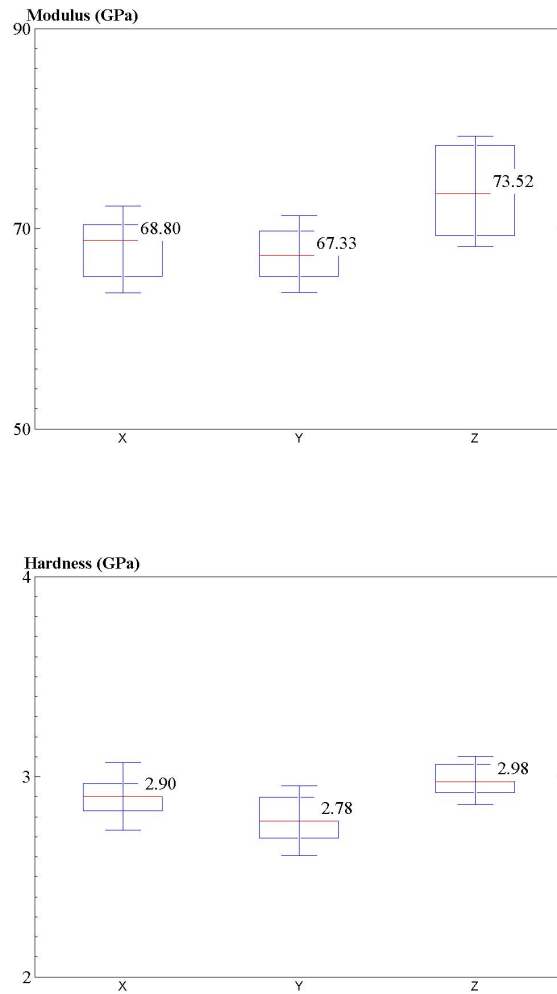
Fig. 18: Relation between Indentation Properties and Orientation; Specimen c0

to the other two faces (Y-face: 67.3 GPa indentation modulus and 2.78 GPa indentation hardness; X-face: 68.8 GPa indentation modulus and 2.90 GPa indentation hardness). Note also the larger spread of moduli (larger box size) on the Z-face compared to the other two faces (Figure 18).

The differences in the median indentation modulus and indentation hardness between Region c0-z and the other two Regions (c0-x and c0-y) suggest a slight pre-existing anisotropy of the intact material. However, Region c0-z also exhibits a greater spread of data for indentation modulus values. Thus, the anisotropy may be overshadowed by the exisitng local variation (i.e., standard deviation) in properties.

Decreased Modulus and Hardness at Grain Boundaries

Grid nanoindentation testing of intact marble (an intact portion of Specimen c1, far from the white patching) reveals lower indentation hardness and indentation modulus values near the boundaries of marble grains. A comparison of a spatial plot of indentation modulus values, a spatial plot of indentation hardness values, and an optical microscopy image illustrates this finding (Figure 19a). The color of each square in the pixel plot corresponds to a particular indentation modulus or indentation hardness value; the highest values are white (90 GPa indentation modulus, and 4.5 GPa indentation hardness), and the lowest values are black (50 GPa indentation modulus, and 1.5 GPa indentation hardness. Note that the indentation modulus and indentation hardness values from all indentations in the grid are shown; thus data displayed includes non-ideal load-depth paths (Section 2.2).

Both the indentation modulus and indentation hardness spatial plots contain a dark line-shaped region in the upper right corner of the plot (Figure 19a). This region corresponds to the grain boundary in the upper right corner of the optical image. In the indentation modulus plot, the region corresponding to the center of the marble grain is very light, and the regions closest to the boundaries are darker; thus, a gradient of values exists between grain boundary and center. Both indentation modulus and indentation hardness plots indicate the grain boundary with a region of low (dark) indentation modulus/hardness values. In contrast to the gradual change of indentation modulus values, there is a more abrupt change in indentation hardness over a relatively small region along the boundary. Process zone marble grains (Figure 19b; nanoindentation grid conducted close to the
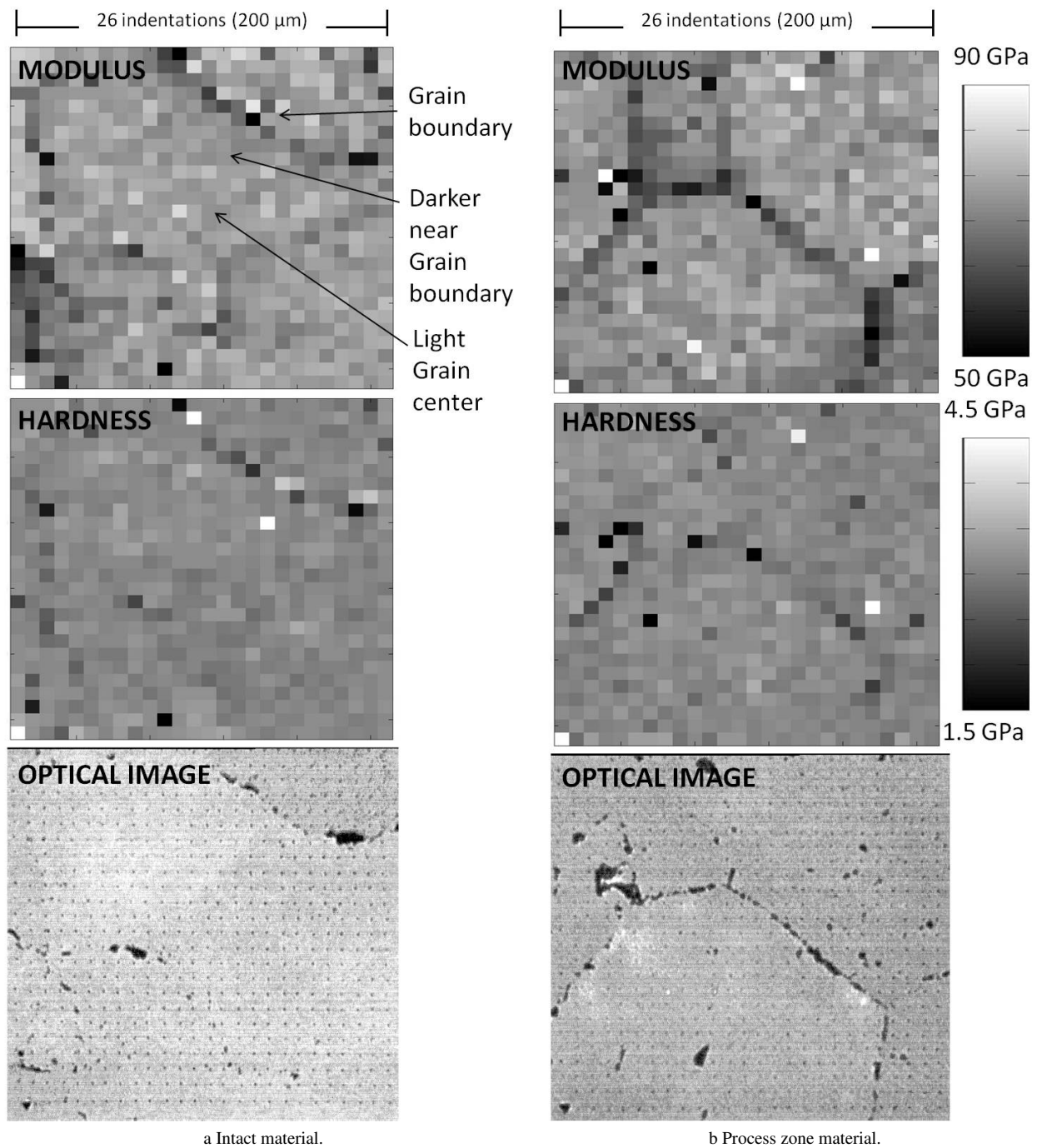
Fig. 19: Comparison of a spatial plot of indentation modulus values, indentation hardness values, and an optical image two different regions.

white patching of Specimen c1) exhibit a more abrupt change in both indentation modulus and indentation hardness at the grain boundary.

Decreased Modulus and Hardness Near Process Zone

Line and grid nanoindentation testing reveals lower indentation modulus values near and within the FPZ (white patching) when compared with indentation modulus values of intact material. Two to three lines (or grids) of 300+ nanoindentations each were placed progressively closer to the FPZ in Regions c1-z1, c1-z2, c1-z3, c1-x, and c2-z.

Proceeding closer to the FPZ (white patching) in Region c1-z1 (Figures 6b, 20), the boxplots drop from a typical indentation modulus of 71.13 GPa farthest from the FPZ, to 67.71 GPa closest to it. Hardness also drops close to the FPZ, with a typical indentation hardness of 3.20 GPa farthest from the FPZ, to 2.73 GPa closest to it.

Proceeding closer to the FPZ (white patching) in Region c1-z2 (Figures 6b, 21), no significant or steady decrease in either nanomechanical property is apparent on this surface. The indentation modulus values peak slightly in the centermost test at 72.89 GPa. This indentation modulus value is just below the typical indentation modulus of intact material on the Z-face (73.52 GPa;
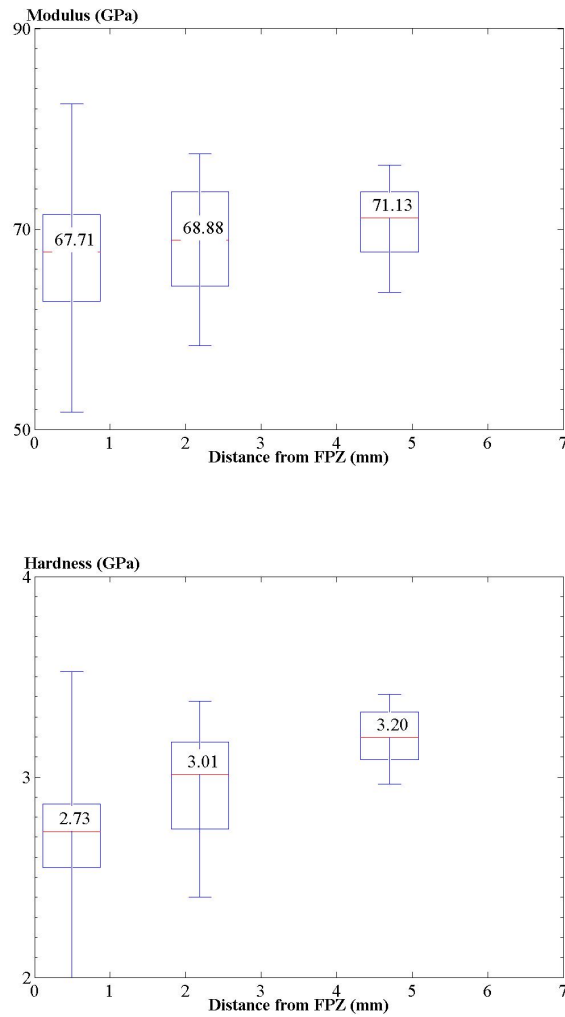
Fig. 20: Relation between Indentation Properties and Distance from Fracture Process Zone (FPZ); Region c1-z1

Modulus plot of Figure 18). The indentation hardnesses are relatively constant around 2.84 GPa, which is also just below the typical indentation hardness value of the Z-face (2.98 GPa, Figure 18).

Proceeding closer the FPZ (white patching) in Region c1-z3, (i.e., parallel to and approximately one centimeter behind Region c1-z2; Figures 6b, 22), no significant decrease in either nanomechanical property is apparent on this specimen. The typical indentation modulus values (67.50 GPa average, Figure 22) lie below the typical moduli of Region c1-z2 (71.2 GPa average, Figure 21), and also lie below the typical indentation modulus of intact material on the Z-face (73.52 GPa; Figure 18). The indentation hardnesses are also relatively constant around an average 2.74 GPa (Figure 22), which lie below the indentation hardness values of Surface Z2 (2.87 GPa average, Figure 21), and also below the typical indentation hardness value of the Z-face (2.98 GPa, Figure 18).

Region c1-x (Figure 6b, 23) shows a slight downward trend of indentation modulus. The surface exhibits a typical indentation modulus of 71.80 GPa farthest from the FPZ, and 68.73 GPa closest to it. The indentation hardnesses are relatively constant, with a typical indentation hardness of 2.65 GPa farthest from the FPZ, and 2.75 GPa closest to it.

Region c2-z (Figure 6c, 24), on a completely different specimen than the other regions just discussed (c1-z1, c1-z2, c1-z3, and c1-x), shows a similar downward trend of indentation modulus and indentation hardness with closeness to the FPZ. Modulus decreases from 66.41 GPa furthest from the FPZ to 63.86 GPa closest to the FPZ. Hardness also decreases from 2.53 GPa furthest from the FPZ to 2.43 GPa closest to the FPZ.

Fig. 21: Relation between Indentation Properties and Distance from FPZ; Region c1-z2

Fig. 22: Relation between Indentation Properties and Distance from FPZ; Region c1-z3
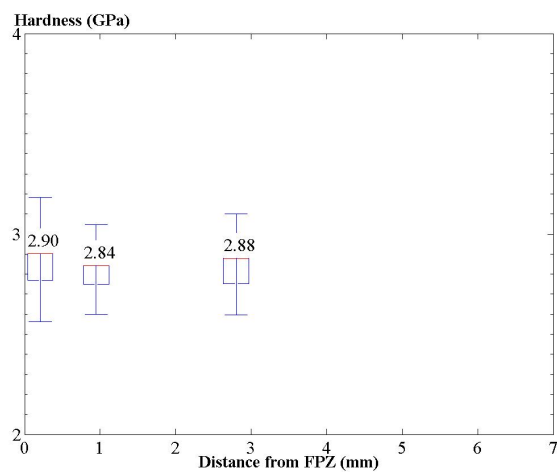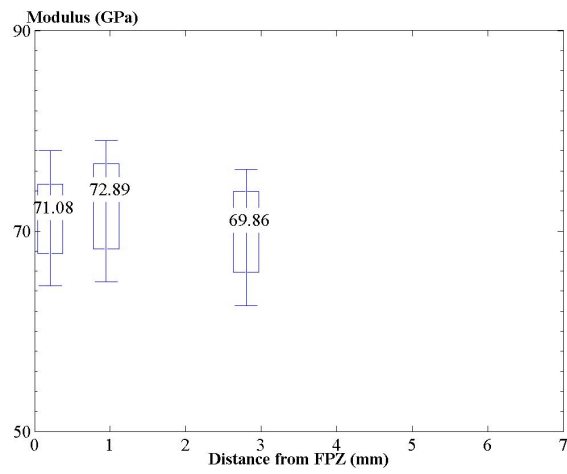
Fig. 23: Relation between Indentation Properties and Distance from FPZ; Region c1-x
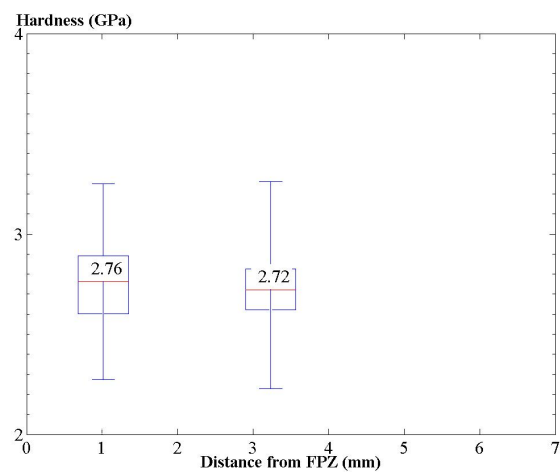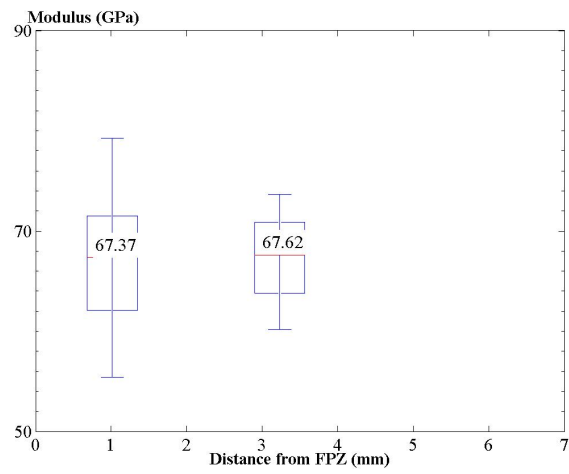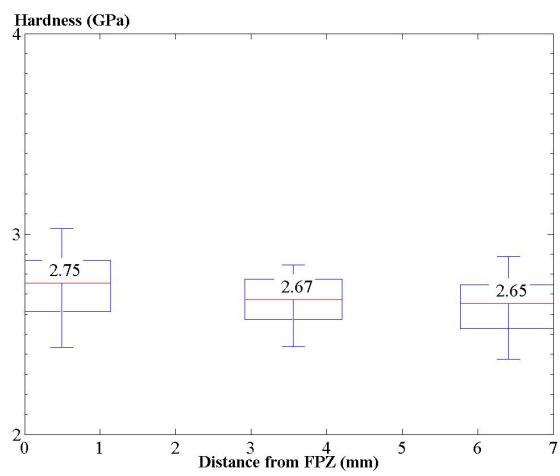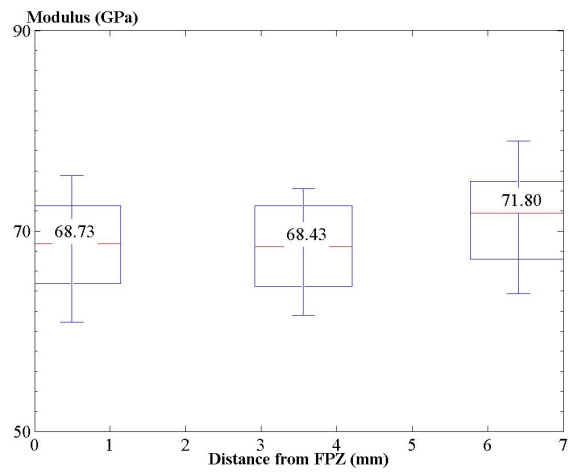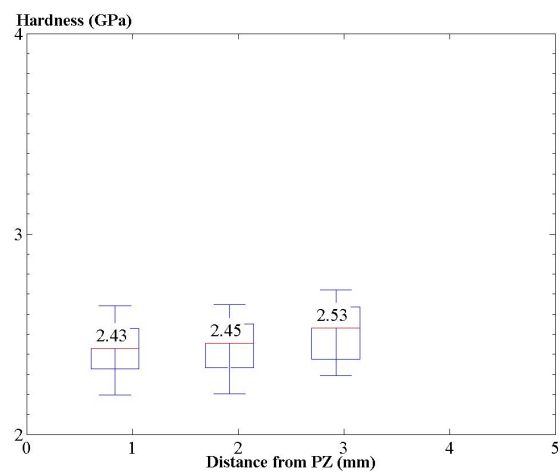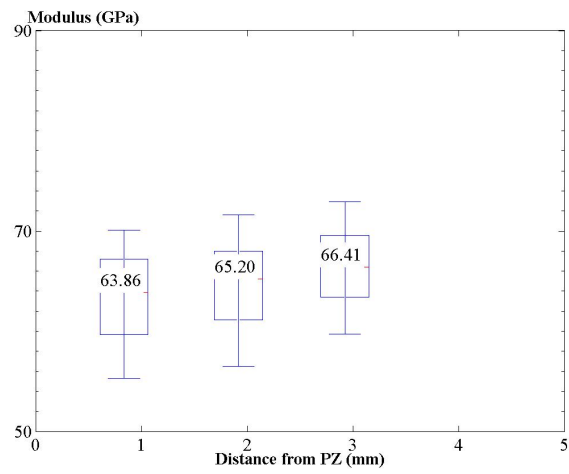
Fig. 24: Relation between Indentation Properties and Distance from FPZ; Region c2-z

4 Interpretation and Discussion

Indentation modulus and indentation hardness link with physical aspects of the tested material. Firstly, indentation hardness is linearly proportional to material yield strength (by a factor of three), as established in the work of Tabor [31]. Hence, change in indentation hardness suggests that the material has changed; a reduction in indentation hardness suggests that the material is weaker.

The indentation modulus links directly with material elasticity. As introduced in Section 1 (Equation 1), indentation modulus is determined from the stiffness S immediately upon unloading. *(Addresses Comment (6).)* For a linear-elastic material, dimensional analysis yields an expression of unloading stiffness by only geometric properties of the indenter probe, and elastic properties of the indented material (for details and derivation, see [33]). In fact, for isotropic materials (as introduced in Section 1), the indentation modulus coincides precisely with the classic plane-stress modulus of elasticity (Equation 3). Elasticity describes material strain in response to an applied stress. A change in elasticity of a material may be induced by a physical defect below the testing scale; this explanation is very likely when the applied load is constant, as in the current investigation. For example, a pre-existing crack in a cement sample will alter the stress-strain behavior of a uniaxial test, and thus alter the derived modulus; similarly, a defect below the scale of indentation may affect the derived indentation modulus. These defects can possibly take the form of cracks with a length scale below indentation depth (≈ 250 nm in this investigation). Thus, nanoindentation modulus provides a means to monitor cracking at or below the scale of indentation. For the current investigation, nanoindentation modulus provides a means to monitor cracking at a scale beneath that accessed by microscopy.

The crack density trends discussed below (Section 4.1) validate previous work on microcracking of Carrara marble [36]. The nanomechanical property trends discussed in Sections 4.2 and 4.3 extend this previous work to a smaller scale, and provide insight into the physical mechanisms at play during the fracture of brittle materials.

4.1 Microstructure of Process Zone

In this investigation, analysis of ESEM images revealed two key features of the FPZ in an unprepared (i.e., non-polished, non-carbon-coated) specimen: microcracks, and spalling. Additionally, images of debris were captured. The microscopy results suggest two interesting conclusions. Firstly, the debris may contribute to the white appearance of the FPZ in marble. Secondly, no single crack density governs the FPZ. As indicated and quantified in the crack density analysis, a variety of densities may be found in FPZ areas. As suggested by the imaging of a failed specimen, loading a specimen beyond the initial appearance of white patching (all the way to failure) can increase the density of microcracking in the FPZ from a maximum of the Medium crack density level (391 µm crack per 100^2 µm^2 of area) to a new maximum of high crack density level (630 µm crack per 100^2 µm^2 of area; Table 3).

Wong [37] identified a similar trend regarding increased crack density: increased crack density in a region surrounding the pre-existing crack, and decreased crack density far from the pre-existing crack, as displayed in Figure 15. Classic fracture mechanics identifies a high-stress region surrounding the initial crack. Thus, although the current investigation did not find a similar "surrounding" nature of crack density – perhaps owing to the different stress states of samples investigated, and to the different sizes of regions investigated (approximately 0.8 mm^2 in Figure 15 from [37], but 4-5 mm^2 in Figures 16 and 17) – both this investigation and [37] agree that a higher stress, whether obtained by loading to failure or by moving closer to the initial crack – yields a higher crack density level.

Although both debris and increased microcrack density may contribute to the white appearance of the FPZ, it is not currently clear which factor contributes more. Analysis of similarly cracked specimens beyond those covered in the current investigation will enhance these conclusions. However, both factors represent material crack damage at the microscale – microcracks. The nanoindentation property trends discussed in the next sections suggest that this crack damage continues at scales smaller than that detected by microscopy.

4.2 Decreased Modulus and Hardness at Grain Boundaries

As indicated in Figures 19a and 19b, both indentation modulus and indentation hardness decrease from grain centers to grain boundaries. Based on the figures, the decreases are approximately 10 GPa (from 75 GPa to 65 GPa, a decrease of about 14%) in the case of indentation modulus, and 0.5 GPa (from 3 GPa to 2.5 GPa, a decrease of about 17%) in the case of indentation hardness. For this study, these decreases are on the same order as the decrease in indentation modulus and indentation hardness near the FPZ, discussed in the following section (Section 4.3). These trends suggest that FPZ and intact grain boundary material have similar strength and elasticity properties. Again, while microcracking near grain boundaries has been found in the literature [35, 37], this study uses a tool – nanoindenation – whose measurements quantitatively correlate these grain-boundary mechanical properties with FPZ mechanical properties.

4.3 Decreased Modulus and Hardness Near Process Zone

Tables 4 and 5 condense the critical information from Figures 20 through 24.

The first five rows of each table present median (and standard deviation) nanoindentation modulus and indentation hardness values from each test. The values in the "Near" column come from the nanoindentation test series closest to the FPZ in each

Table 4: Summary of nanoindentation modulus values (median ± standard deviation) from all FPZ regions.

	INDENTATION MODULUS				
Region	**Near (GPa**	**Middle (GPa)**	**Far (GPa)**	**Decrease (%)**	**|t|**
c1-z1	67.71 ±15.40	68.88 ±9.58	71.13 ±6.35	4.8%	2.95
c1-z2	71.08 ±6.76	72.89 ±7.04	69.86 ±6.78	-1.8%	3.77
c1-z3	67.37 ±11.92	–	67.62 ±6.75	0.4%	(0.64)
c1-x	68.73 ±7.32	68.43 ±6.30	71.80 ±7.60	4.3%	5.55
c2-z	63.86 ±7.39	65.20 ±7.56	66.41 ±6.61	3.9%	5.45
Average	**67.7** ±10.6	**68.2** ±8.2	**68.7** ±7.1	1.5%	3.28

Table 5: Summary of nanoindentation hardness values (median ± standard deviation) from all FPZ regions.

	INDENTATION HARDNESS				
Region	**Near (GPa**	**Middle (GPa)**	**Far (GPa)**	**Decrease (%)**	**|t|**
c1-z1	2.73 ±0.77	3.01 ±0.49	3.20 ±0.22	14.7%	9.15
c1-z2	2.90 ±0.31	2.84 ±0.22	2.88 ±0.25	-0.7%	(1.11)
c1-z3	2.76 ±0.49	–	2.72 ±0.52	-1.5%	(0.46)
c1-x	2.75 ±0.30	2.67 ±0.20	2.65 ±0.26	-3.8%	4.60
c2-z	2.43 ±0.22	2.45 ±0.22	2.53 ±0.21	4.0%	4.28
Average	**2.7** ±0.5	**2.7** ±0.3	**2.8** ±0.4	3.5%	4.36

Region (within approximately 1 mm in most Regions). The values in the "Far" column come from the nanoindenation test series furthest from the FPZ in each Region (greater than 2.5 mm on all Regions). The values in the "Middle" column come from the nanoindentation test series located between the "Near" series and the "Far" series. (The precise locations of each test series are seen in Figures 20 through 24.) A statistical analysis is given in the final columns of Tables 4 and 5. In the "Decrease" columns, the decrease in indentation values between the "Far" test series and the "Near" test series is shown. In the "$|t|$" columns, the tables present the statistical significance of the decrease in indentation hardness and indentation modulus with the t-statistic:

$$s^2 = \frac{(n_1 - 1)s_1^2 + (n_2 - 1)s_2^2}{n_1 + n_2 - 2} \tag{5}$$

$$t = \frac{x_1 - x_2}{s\sqrt{\frac{1}{n_1} + \frac{1}{n_2}}} \tag{6}$$

where s_1 and s_2 are the standard deviations of the two indentation test series compared, n_1 and n_2 are the counts of the two test series, and x_1 and x_2 are the sample means of the test series. A decrease is statistically significant when the calculated $|t|$-statistic follows $|t| > 1.66$. The final row in each table presents the average and standard deviation of values from all regions, as listed in the rows directly above.

As shown in Tables 4 and 5, both indentation modulus and indentation hardness decrease in the FPZ specimens as the nanoindentation line approaches the FPZ. The statistical analysis presented in Tables 4 and 5 illuminates these trends. Statistically significant t-statistics are found: in Region c1-z1 for the decrease in indentation modulus and indentation hardness; in Region c1-z2 for the increase in indentation modulus; in Region c1-x for the decrease in indentation modulus and increase in indentation hardness; and in Region c2-z for the decrease in indentation modulus and indentation hardness. Thus, although there are some discrepancies, a statistically significant decrease of indentation modulus and indentation hardness can be observed in many of the regions as one gets closer to the FPZ.

The final rows of Tables 4 and 5 collectively analyze results on all regions. The "Average" rows present the average (mean) values and standard deviation of all combined individual tests in the rows above. Thus, the rows present an average of nanomechanical properties within 1 mm of the FPZ ("Near" column), greater than 2.5 mm from the FPZ ("Far" column), and at a distance somewhere between those distances. The values in these rows show a statistically significant reduction in indentation modulus and indentation hardness with closeness to the FPZ for combined nanoindentation values across two different FPZ specimens. Modulus values in aggregate show a statistically significant reduction of 1.5%, and indentation hardness values in aggregate show a statistically significant reduction of 3.5% between values from the "Far" test series and those from the "Near" test series.

Note that the decrease on average (i.e., in the final row) is small for both modulus and hardness, and below the standard deviation in the case of indentation modulus. However, three factors suggest the importance of this relatively small decrease. Firstly, the t-statistic analysis suggests that there is a significant probability that the difference between the values of the test populations is due to real phenomena, and not due to random chance. Secondly, this decrease represents a trend derived from thousands of individual indentations. This trend thus holds across a large number of individual mechanical tests. Hence, the large number of tests and the statistical significance suggest that a real phenomenon is affecting the properties within the FPZ. Thirdly, certain regions showed a greater average decrease in indentation modulus and hardness – specifically, regions c1-z1 and c2-z. Thus, the trend exists on certain specimens. Specimens similar to c1-z1 and c2-z may be useful for further study of the indentation modulus and hardness reduction trend. Thus, under the consideration of these three factors, the statistical analysis in Tables 4 and 5 suggests

that real small-scale phenomena are occurring and affecting FPZ Carrara marble. *(Addresses Comment (7).)* The technique used to identify this trend – nanoindenation – suggests the nature of two phenomena which are possibly occuring:

(i) Change in strength

(ii) Modulus reduction, at a scale smaller than the indentation depth; i.e., here less than 250 nm.

The next sections explain these phenomena.

Change in Strength

Nanoindentation results point to a reduction in indentation hardness near the FPZ (by nearly 15% on Region c1-z1, to below 3 GPaon Regions c1-z3, c1-z2, c1-x, and c2-z, and by 3.5% overall, Table 5). In fact, both grain boundaries and FPZ material exhibit low indentation hardnesses (below 3 GPa, light gray in Figure 19a). This similarity between FPZ indentation hardness values and intact grain boundary indentation hardness values suggest that otherwise weakened FPZ material is physically similar to the weakened material at grain boundaries in intact material (discussed in the next section) with respect to material properties.

Modulus Reduction, at a Scale Smaller Than the Indentation Depth

Most results point to a reduction in indentation modulus near the FPZ (by 4.8% on Region c1-z1, to below 68 GPaon Regions c1-z1, c1-z3, and c2-z, and by 1.5% in aggregate, Table 4). Again, both grain boundaries and FPZ material exhibit low indentation modulus values (below ≈ 68 GPa, light gray in Figure 19a). Based on the comments made at the beginning of Section 4, this indentation modulus reduction reflects nanostructurally damaged material. Previous work has identified macro- and microscale damage within the FPZ [37]. The current investigation has used nanoindentation to identify damage at a smaller scale than that found with microscopy.

The precise determination of the extent of nanocracking of FPZ material remains the subject of future investigations. Two methods exist to make this determination: to vary the depth of nanoindentation, and to collectively assess both nanoindentation values and locations. Firstly, the depth of nanoindentation identifies the maximum size of nanocrack: nanocracks must be smaller than the depth of nanoindentation in order to effect a reduction in measured nanomechanical properties. Thus, nanoindentations to varying depths may identifiy a minimum size of nanocrack. Further nanoindentation testing can thus identify a precise range of nanoscale material damage size. Secondly, the location on the specimen (i.e., distance from white patching) at which nanoindentation modulus values return to those of intact material may indicate the boundary of the nanocracked zone. Thus, nanoindentation testing over a larger area can confirm the size of nanocracked zone for a particular specimen and loading conditions.

5 Summary and Conclusions

Very importantly, this work has developed and applied a combined nanoindentation-microscopy technique for exploring fundamental (i.e., grain-scale) FPZ properties of quasi-brittle materials both near the FPZ and at grain boundaries. This is the first investigation to use this technique in natural geomaterials.*(Addresses Comment (2).)* This study combined microscopic observation with nanoindentation to investigate intact Carrara marble and the effects of the FPZ. The work specifically compared:

1. different orientations of the marble block,
2. grain center and grain boundary marble (in both "intact" and FPZ regions), and
3. "intact" and FPZ marble.

The work revealed one microscale trend:

1. Increase in crack density with increased loading,

and two major nanoscale trends:

2. Reduced nanoindentation modulus and hardness with closeness to the process zone
3. Reduced nanoindentation modulus and hardness with closeness to grain boundaries

These three trends highlight the major contributions of this work. The combination of microscopy and nanoindentation confirmed the established fact of increased crack density near the FPZ, and then showed that an analogous weakness occurs at a smaller scale near the FPZ and near grain boundaries. The apparent similarity in nanoscale mechanical properties in the FPZ and near grain boundaries indicates that the observed material behavior represents fundamental characteristics.

While these results are very important by themselves, they indicate where further work is necessary: to investigate the nanoscale properties of the FPZ at different depths, and in other quasi-brittle materials. Such experiments could better clarify whether the process zone property trends occur mainly in Carrara marble and similar geomaterials, or extend to highly heterogeneous systems such as granite and concrete. Nevertheless, the work has ultimately shown the effectiveness of a relatively new combination of techniques – nanoindentation and microscopy – for investigating small-scale, and thus previously inaccessible, properties of fractured natural geomaterials. This study thus lays an important stepping stone in the path towards more investigation and understanding of quasi-brittle material behavior at fundamental grain scales. *(Addresses Comment (2).)*

Appendices

A Surface Preparation for Nanoindentation

Surface preparation is vital for nanoindentation. An ideal surface is smooth and flat, and models the infinite half-space assumed in Equations 1 and 2. A non-ideal surface is "rough", or contains raised and depressed regions) on the surface. The properties derived from nanoindentation on a non-ideal surface exhibit greater spread with surface roughness [23]. Polishing, or rubbing the sample surface with abrasives in stages of decreasing abrasive size, reduces roughness and thereby produces more accurate nanoindentation results. Each nanoindentation specimen in the current investigation underwent a five-stage polishing procedure before nanoindentation testing [5, 23] (Table 6).

Table 6: Specimen surfaces are prepared for nanoindentation with a five-stage polishing procedure.

Stage	Abrasive Size (μm)	Abrasive Type	Lubricant	Duration
1	76	Silicon Carbide	none	5 min
2	22	Aluminum Oxide	none	5 min
3	9	Diamond	Oil	5 min
4	3	Diamond	Oil	5 min
5	0.25	Diamond	Oil	9 hr

The Asylum Research MFP-3D Atomic Force Microscope© was used to verify the adequacy of this polishing procedure. Following statistical corrections for surface sloping and large scale surface waviness, the final roughness, R_q, was determined from (via Mountains SPM Image Analysis Software; Figure 25):

$$R_q = \sqrt{\frac{1}{n^2} \sum_{i=1}^{n} \sum_{j=1}^{n} z_{ij}^2}, \tag{7}$$

where n is the number of pixels along the edge of the AFM scan (Figure 25; each μm contains a number of pixels set by the scan resolution), and z_{ij} is the height at a position (i, j) above or below a mean reference plane [23]. The scans in this investigation had a resolution of 40 pixels by 40 pixels, and a size of 50 μm by 50 μm. Essentially, the roughness value represents the average distance from a reference level near the sample surface to the highest peaks or the deepest valleys on the surface. Figure 25 (c) depicts the topographical information from a single scan; the dark line through the middle represents the reference level. Roughness is formulated with respect to distances from this datum. This yielded a final roughness of $R_q = 9.32$ nm.
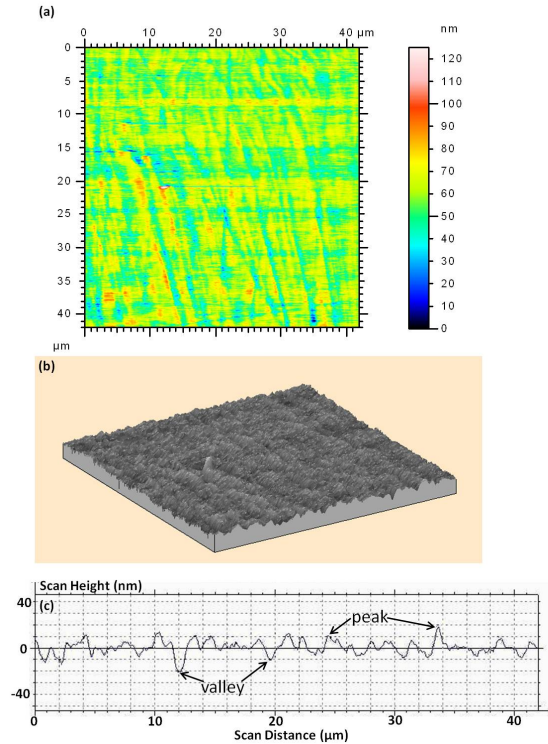

Fig. 25: An AFM scan yields (a) a color-gradient contour plot of the surface, which may also be displayed as (b) a 3D isometric diagram. (c) depicts height information from a single scan with respect to a reference level, or datum.

Surface roughness should be less than five times the depth of nanoindentation [23]. In this investigation, the surface roughness of 9.32 nm is far less than five times the depth of nanoindentation – 250 nm. Thus, the surface preparation employed in this investigation is sufficient.

B Nanoindentation Parameter Selection

Table 7: A comparison of typical indentations and a large-load "exaggerated" indentation.

	"Exaggerated" Indentation	Typical Indentation
P_{max} mN	250	2.85
Depth of Indentation, nm	2800	240
Inter-indentation Spacing, μm	—	8
Length of Indentation-induced Fracture, μm	<17.2	negligible

The selection of two nanoindentation parameters – load applied by the nanoindenter and spacing between indentations – affects the accuracy of nanoindentation results. If the load is too high or spacing too small, indentation-induced fractures may extend from one indentation to the next and influence the derived mechanical properties.

The appropriateness of the nanoindentation parameters was verified with ESEM. An investigation was conducted to see whether indentation-induced fracture occurred for the indentation parameters used in the study. Two types of indentations were conducted – typical indentations with parameters used through the current study, and "exaggerated" indentations with a much higher (by a factor of 80) indentation load (see Table 7). It was found that no indentation-induced fracture was apparent for typical indentations. It was also found that the "exaggerated" indentations induced fracture extending only 17.2 μm, or nearly twice the typical indentation spacing. It is thus assumed that the typical indentation load of 2.85 mN avoids indentation-induced fracture, and a spacing of 8 μm prevents indentations from running into any potential fracture.
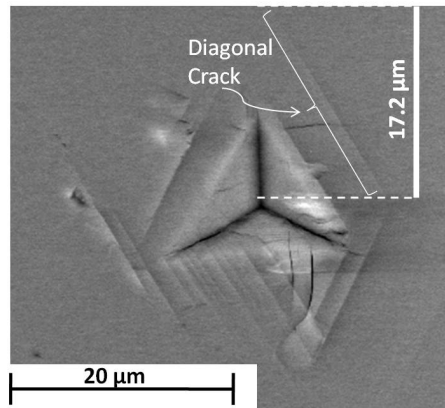

Fig. 26: An "exaggerated" indentation shows little indentation- induced cracking. The greatest observable distance of cracking from the center of the indentation is 17.2 μm(between center of indentation and tip of diagonal crack).

C Nanoindentation Boxplots

A box plot provides a first-order means of data analysis for this investigation because it presents a concise summary of the spread and typical values of each nanoindentation test (where a single test consists of over 300 individual nanoindentations). Although box plots may assume various forms and present various statistical parameters, for the data in this investigation the bottom and top of the whiskers correspond to the mean nanoindentation value (either modulus or hardness), respectively minus and plus one standard deviation. The central value corresponds to the median value, and the bottom and top of the box correspond to the 25th and 75th percentile of the data. Median is used since it expresses the typical value from many nanoindentations without being susceptible to outlier values, in the way that mean is susceptible. Note that for normally distributed data sets, approximately 25% of the data can be found between the mean and the 25th or 75th percentile. The closeness of the ends of the box (25th/75th percentile) to the ends of the whiskers (average +/- one standard deviation) indicates the spread of the data. Data sets with little spread will have larger boxes, and smaller distances from box to whiskers; data sets with more spread will have larger boxes, and greater distances from box to whiskers. The box plot thus presents a concise summary of the spread and typical values of the data from each nanoindentation test series.
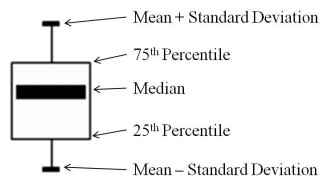
Fig. 27: A box plot succinctly captures the spread and typical value of a test comprised of many individual nanoindentations.

References

1. Alber M, Brardt A (2003) Factors influencing fracture toughness kic from simple screening tests. Int J Rock Mech Min 40(5):779–784
2. Alber M, Hauptfleisch U (1999) Generation and visualization of microfractures in carrara marble for estimating fracture toughness, fracture shear and fracture normal stiffness. Int J Rock Mech Min 36(8):1065–1071
3. Anders MH, Wiltschko DV (1994) Microfracturing, paleostress and the growth of faults. J Struct Geol 16(6):795–815
4. Atkinson BK (1979) Fracture toughness of tennessee sandstone and carrara marble using the double torsion testing method. Int J Rock Mech Min 16(1):49–53
5. Austin NJ (2008) Grain size evolution and strain localization in deformed marbles. Dissertation, Massachusetts Institute of Technology
6. Backers T, Stanchits S, Dresen G (2005) Tensile fracture propagation and acoustic emission activity in sandstone: The effect of loading rate. Int J Rock Mech Min 42(7-8):1094–1101
7. Bulychev SI, Alekhin VP, Shorshorov MK, Ternovskii AP (1976) Mechanical properties of materials studied from kinetic diagrams of load versus depth of impression during microimpression. Problemy Prochnosti 9:79–83
8. Bulychev SI, Alekhin VP, Shorshorov MK, Ternovskii AP, Shnyrev GD (1976) Determining young's modulus from the indentor penetration diagram. Ind Lab pp 1409–1412
9. Butenuth C, Freitas MHD, Al-Samahiji D, Park HD, Cosgrove JW, Schetelig K (1993) Observations on the measurement of tensile strength using the hoop test. Int J Rock Mech Min 30(2):157–162
10. Chengyong W, Peide L, Rongsheng H, Xiutang S (1990) Study of the fracture process zone in rock by laser speckle interferometry. Int J Rock Mech Min 27(1):65
11. Denarie E, Saouma VE, Iocco A, Varelas D (2001) Concrete fracture process zone characterization with fiber optics. J Eng Mech pp 494–502
12. Du JJ, Kobayashi AS, Hawkins NM (1990) An experimental-numerical analysis of fracture process zone in concrete fracture specimens. Eng Fract Mech 35(1-3):15–27
13. Ganneau FP, Constantinides G, Ulm FJ (2006) Dual-indentation technique for the assessment of strength properties of cohesive-frictional materials. Int J Solids Struct 43(6):1727–1745
14. Guo ZK, Kobayashi AS, Hawkins NM (1993) Further studies on fracture process zone for mode i concrete fracture. Eng Fract Mech 46(6):1041–1049
15. Hertzberg RW (1996) Deformation and fracture mechanics of engineering materials, 4th edn. John Wiley & Sons, Inc.
16. Irwin GR (1957) Analysis of stresses and strains near the end of a crack traversing a plate. J Appl Mech (24):361–364
17. Jaeger JC (1967) Failure of rocks under tensile conditions. Int J Rock Mech Min 4(2):219–227
18. Janssen, Wagner, Zang, Dresen (2001) Fracture process zone in granite: a microstructural analysis. Int J Earth Sci 90(1):46–59
19. Labuz JF, Shah SP, Dowding CH (1983) Post peak tensile load-displacement response and the fracture process zone in rock. In: 24th U.S. Symposium on Rock Mechanics., pp 421–428
20. Labuz JF, Shah SP, Dowding CH (1987) The fracture process zone in granite: evidence and effect. Int J Rock Mech Min 24(4):235–246
21. Lin Q, Fakhimi A, Haggerty M, Labuz JF (2009) Initiation of tensile and mixed-mode fracture in sandstone. Int J Rock Mech Min 46(3):489–497
22. Marini P, Bellopede R (2009) Bowing of marble slabs: Evolution and correlation with mechanical decay. Constr Build Mater 23(7):2599–2605
23. Miller M, Bobko C, Vandamme M, Ulm FJ (2008) Surface roughness criteria for cement paste nanoindentation. Cement Concrete Res 38:467–476
24. Molli G, Conti P, Giorgetti G, Meccheri M, Oesterling N (2000) Microfabric study on the deformational and thermal history of the alpi apuane marbles (carrara marbles), italy. J Struct Geol 22:1809–1825
25. Nasseri MHB, Mohanty B, Young RP (2006) Fracture Toughness Measurements and Acoustic Emission Activity in Brittle Rocks, Birkhuser Basel, pp 917–945. Rock Damage and Fluid Transport, Part I
26. Oliver W, Pharr G (1992) An improved technique for determining hardness and elastic modulus using load and displacement sensing indentation experiments. J Mater Res 7(6):1564–1583
27. Otsuka K, Date H (2000) Fracture process zone in concrete tension specimen. Eng Fract Mech 65(2-3):111–131
28. Picart P, Diouf B, Lolive E, Berthelot JM (2004) Investigation of fracture mechanisms in resin concrete using spatially multiplexed digital fresnel holograms. Opt Eng 43:1169–1176
29. Pique EJ, Dortmans L, de With G (2003) A model material approach to the study of fracture process zone of quasi-brittle materials. J Mater Sci 38(19):4003–4011
30. Swanson PL, Spetzler H (1984) Ultrasonic probing of the fracture process zone in rock using surface waves. U.S. National Symposium on Rock Mechanics, 25th, Northwestern University, Evanston, IL, June 25-27, 1984, Paper. 10 p. Sponsorship: U.S. Geological Survey.
31. Tabor D (1948) A simple theory of static and dynamic hardness. P Roy Soc A – Math Phy 192(1029):247–274
32. Uguz A, Martin JW (1996) Plastic zone size measurement techniques for metallic materials. Mater Charact 37:105–118
33. Vandamme M (2008) The nanogranular origin of concrete creep: a nanoindentation investigation of microstructure and fundamental properties of calcium-silicate-hydrates. Dissertation, Massachusetts Institute of Technology
34. Wong LNY, Einstein HH (2009) Using high speed video imaging in the study of cracking processes of rock. Geotech Test J 32(2):1–17
35. Wong NY (2008) Crack coalescence in molded gypsum and carrara marble. Dissertation, Massachusetts Institute of Technology
36. Wong NY (2009) Crack coalescence in molded gypsum and carrara marble: Part 1. macroscopic observations and interpretation. Rock Mech Rock Eng (42):475–511
37. Wong NY (2009) Crack coalescence in molded gypsum and carrara marble: Part 2 – microscopic observations and interpretation. Rock Mech Rock Eng (42):513–545
38. Zang A, Wagner FC, Stanchits S, Janssen C, Dresen G (2000) Fracture process zone in granite. J Geophys Res 105:23,651–23,662
39. Zhang ZX (2002) An empirical relation between mode i fracture toughness and the tensile strength of rock. Int J Rock Mech Min 39(3):401–406
40. Zietlow WK, Labuz JF (1998) Measurement of the intrinsic process zone in rock using acoustic emission. Int J Rock Mech Min 35(3):291–299